# OVERPARAMETRIZATION BENDS THE LANDSCAPE: BBP TRANSITIONS AT INITIALIZATION IN SIMPLE NEURAL NETWORKS

**Anonymous authors**Paper under double-blind review

000

001

003

004

006

008 009 010

011

013

014

015

016

017

018

019

021

025

026

027

028

029

031 032 033

034

037

038

040

041

042

043

044

045

046

047

048

051

052

#### **ABSTRACT**

High-dimensional non-convex loss landscapes play a central role in the theory of Machine Learning. Gaining insight into how these landscapes interact with gradient-based optimization methods, even in relatively simple models, can shed light on this enigmatic feature of neural networks. In this work, we will focus on a prototypical simple learning problem, which generalizes the Phase Retrieval inference problem by allowing the exploration of overparametrized settings. Using techniques from field theory, we analyze the spectrum of the Hessian at initialization and identify a Baik-Ben Arous-Péché (BBP) transition in the amount of data that separates regimes where the initialization is informative or uninformative about a planted signal of a teacher-student setup. Crucially, we demonstrate how overparameterization can bend the loss landscape, shifting the transition point, even reaching the information-theoretic weak-recovery threshold in the large overparameterization limit, while also altering its qualitative nature. We distinguish between continuous and discontinuous BBP transitions and support our analytical predictions with simulations, examining how they compare to the finite-N behavior. In the case of discontinuous BBP transitions strong finite-N corrections allow the retrieval of information at a signal-to-noise ratio (SNR) smaller than the predicted BBP transition. In these cases we provide estimates for a new lower SNR threshold that marks the point at which initialization becomes entirely uninformative.

#### 1 Introduction

The geometry of high-dimensional, non-convex loss, risk, or cost landscapes plays a central role in modern machine learning and data science. Such landscapes hide important structural features of the data into specific local structures and mostly deep configurations. Despite their complexity, the optimization of these landscapes is typically performed using local iterative algorithms, most notably gradient descent and its stochastic variants. Understanding the success and limitations of these algorithms remains a fundamental open problem. It has been first observed that in regimes where the dataset is large relative to the problem dimension N, i.e., at high signal-to-noise ratio (SNR), the landscape can undergo an effective trivialization, becoming nearly convex and devoid of spurious local minima (Fyodorov, 2004; Soudry & Carmon, 2016; Cai et al., 2022). In this setting, each point in the landscape contains a clear directional signal guiding the optimization toward informative minima. Furthermore, it has been widely reported that overparameterization of the learning model can induce a smoothing of the loss landscape even in regimes with moderate or low SNR, thereby facilitating optimization (Shevchenko & Mondelli, 2020; Cooper, 2021). Perhaps more surprisingly, even in settings where spurious non-informative minima remain prevalent, gradient-based methods often still succeed (Baity-Jesi et al., 2018; Liu et al., 2020; Ros et al., 2019; Mannelli et al., 2019). This apparent paradox has been addressed in a series of works on high-dimensional inference problems such as matrix-tensor PCA (Sarao Mannelli et al., 2019) and phase retrieval (Sarao Mannelli et al., 2020a). These studies reveal that gradient flow dynamics can avoid these poor solutions due to the local geometry of high-dimensional basins of attraction, which are typically explored by the dynamics. The high dimensional basins of attraction of gradient flow, although still non informative themselves, develop an instability towards the signal at relatively low SNR. This phenomenon is

sometimes referred to as the "blessing of dimensionality". Crucially, the emergence of such instabilities at increasing SNR is associated with a qualitative change in the spectrum of the local Hessian in a transition known as the Baik–Ben Arous–Péché (BBP) transition (Baik et al., 2005).

Alternative learning approaches, mostly applied to signal reconstruction problems, are based on the use of spectral methods (Netrapalli et al., 2013; Montanari & Sun, 2018) to define a warm start to subsequent local iterative algorithms, with the aim of boosting their performances. Typically, in spectral methods such initial guess is provided by the leading eigenvector of a matrix, which is a function of the input data tailored to the structure of the specific problem (Montanari & Sun, 2018; Lu & Li, 2020; Mondelli & Montanari, 2018; Maillard et al., 2022). Interestingly in some cases, for instance phase retrieval or tensor PCA, such ad hoc procedure can be also linked to the risk landscape as the matrix used for spectral initialization corresponds to the negative Hessian of a suitably defined cost function evaluated at random configurations and averaged over many of them (Biroli et al., 2020). Therefore its leading eigenvector represents the direction with the most negative (or smallest positive) curvature found at the initial condition in such averaged landscape. Also in this case, when the SNR increases, the spectrum of such matrix undergoes a BBP transition, after which the leading eigenvector develops a finite correlation with the signal. A similar phenomenon occurs in the Hessian of the cost function evaluated at individual random configurations (Bonnaire et al., 2024; Arous et al., 2025), but it is less known how this landscape feature is also affected by overparametrization. Moreover, very recent work (Bonnaire et al., 2024) has shown that the information contained in the curvature of the landscape in random configurations, for finite input dimensions N, could further automatically help gradient-based methods in finding the deep informative minima. The interplay between the gradient flow algorithmic transitions and the emergence of the signal in the Hessian at the initial condition then defines an effective algorithmic transition in the SNR, which slowly changes with the dimensionality of the data set. This already nontrivial mechanism may be further modified in the presence of overparameterization, motivating a deeper exploration of its role in shaping the optimization landscape and the dynamics therein.

In this work, we consider an extended version of the classical phase retrieval problem by focusing on a teacher-student setting based on two-layer soft-committee machines with quadratic activations. The widths of the hidden layers of the student and teacher networks, denoted by p and  $p^*$  respectively, are generic and finite, while the dimensionality N of the input samples will be considered very large and diverging, except in numerical tests. When  $p=p^*=1$ , the setting reduces to the standard phase retrieval problem, which involves recovering a hidden signal from magnitude-only projections. It notoriously results in a non-convex optimization problem with broad relevance in optics (Millane, 1990), signal processing (Bendory et al., 2017), quantum mechanics (Orl et al., 1994), and which has often served as a prototypical example for exploring the interplay between optimization dynamics and high-dimensional geometry (Sun et al., 2018).

For general p and  $p^*$ , and in particular for  $p > p^*$  we explore the effect of overparametrization on the landscape structure. In particular, we focus on the information contained in the local curvature in random positions of a suitably defined class of loss landscapes spanned by a parameter a. We study how it changes with a, p and  $p^*$ . As previously mentioned, the Hessian at initialization could contain more information than expected, which could lower the SNR of algorithmic transitions for gradient-based algorithms, or could be explicitly used in a sort of generalized spectral method.

Our analysis shows that overparametrization generally shifts the BBP transition in the Hessian spectra of random configurations toward lower SNR. The corresponding spectral initialization method based on such local Hessian matrices is therefore expected to extract information earlier than in the underparametrized case and even gradient-based learning dynamics is expected to work better with overparametrization in finite-dimensional practical implementations of the problem. However, we also obtain that in few very specific instances overparametrization may slightly harm the efficiency of signal recovery obtained through the diagonalization of the Hessian at initialization. We also observe that the nature of the BBP transition changes from underparametrized students to students benefitting from overparametrization. When overparametrization increases the standard BBP transition tends to be replaced by a BBP transition associated with a discontinuous jump in the amount of information retrieved. The emergence of discontinuous BBP transitions has been only very recently discussed in association to signal reconstruction in phase retrieval problems (Bocchi et al., 2025a; Bousseyroux & Potters, 2024), and previously only conjectured on theoretical grounds (Potters & Bouchaud, 2020). With this work, we illustrate how they become central when phase retrieval is generalized to an overparametrized learning setup. Moreover, strong finite size effects are expected

to affect numerical observation of discontinuous BBP transitions (Bocchi et al., 2025a). We highlight this aspect in the results of the signal recovery in the overparametrized cases. Interestingly, we observe that higher overparametrization renders the transition more discontinuous. This effect tends to counterbalance the small shift to higher SNR of the signal recovery transition—in the large dimensional limit—obtained at higher overparametrization in specific instances, effectively reinstating a generalized advantage of overparametrization in realistic applications. Finally, we discuss the large overparametrization limit  $p \to \infty$  for fixed  $p^*$  and we reobtain the weak recovery algorithmic transition at an SNR equal to  $p^*/2$ , already discussed in the literature for  $p^*=1$  in Mondelli & Montanari (2018) and for  $p^*>1$  in the Bayes optimal setting in Maillard et al. (2024).

### 2 The model

The teacher–student framework provides a simplified yet powerful setting for studying supervised learning. In this setup, a student network  $\hat{y}(\mathbf{x}): \mathbb{R}^N \to \mathbb{R}$  is trained to match the outputs of an unknown teacher function  $y(\mathbf{x}): \mathbb{R}^N \to \mathbb{R}$  using a set of  $M = \alpha N$  labeled examples. These examples consist of input vectors  $\{\mathbf{x}^\mu\}_{\mu=1}^M$  drawn independently from a Gaussian distribution  $\mathcal{N}(0, \mathbb{I}_N/N)$ , along with their corresponding teacher outputs  $y^\mu = y(\mathbf{x}^\mu)$ . In the case of soft-committee machines with quadratic activations, for a given input vector  $\mathbf{x}^\mu$ , the output of the teacher network is:

$$y(\mathbf{x}^{\mu}) = \frac{1}{p^*} \sum_{l=1}^{p^*} (\mathbf{w}_l^* \cdot \mathbf{x}^{\mu})^2 \equiv \frac{1}{p^*} \sum_{l=1}^{p^*} (u_l^{\mu})^2,$$
(1)

where  $p^*$  is the width of the hidden layer of the teacher network and  $u_l^{\mu} \equiv \mathbf{w}_l^* \cdot \mathbf{x}^{\mu}$  is the preactivation output of the l-th teacher node  $\mathbf{w}_l^*$ . Each teacher node  $\mathbf{w}_l^*$  is independently sampled from the sphere  $S_{N-1}(\sqrt{N})$ . Similarly, the output of the student network is defined as:

$$\hat{y}(\mathbf{x}^{\mu}) = \frac{1}{p} \sum_{k=1}^{p} (\mathbf{w}_k \cdot \mathbf{x}^{\mu})^2 \equiv \frac{1}{p} \sum_{k=1}^{p} (\lambda_k^{\mu})^2,$$
 (2)

where p is the width of the hidden layer of the student network and  $\lambda_k^{\mu} \equiv \mathbf{w}_k \cdot \mathbf{x}^{\mu}$  is the pre-activation output of the k-th student node  $\mathbf{w}_k$ . Standard gradient descent algorithms iteratively modify the weights  $\{\mathbf{w}_k\}_{k=1}^p$  to minimize an empirical loss on the training data  $\{\mathbf{x}^{\mu}\}_{\mu=1}^M$ . Following previous works (Bonnaire et al., 2024), we define a family of normalized quadratic loss functions:

$$\mathcal{L}_{\mathbf{w}} = \sum_{\mu=1}^{M=\alpha N} \ell_{\mathbf{w}}(\mathbf{x}^{\mu}) \equiv \frac{1}{2} \sum_{\mu=1}^{M=\alpha N} \frac{\left[y(\mathbf{x}^{\mu}) - \hat{y}(\mathbf{x}^{\mu})\right]^2}{a + y(\mathbf{x}^{\mu})},\tag{3}$$

where the parameter a>0 controls the strength of the normalization that prevents pathologies due to rare very small or very large teacher outputs. By regulating the conditioning of the Hessian eigenspectrum, the denominator ensures the appearance of a hard left edge, an essential feature for our analytical analysis.

Instead of studying the dynamics of the learning process, we focus here on the structure of the loss landscape itself. In particular, we are interested in the local curvature of the empirical loss at initialization, which is governed by the spectral properties of its Hessian matrix  $\mathcal{H} \in \mathbb{R}^{pN \times pN}$ . This can be seen as a block matrix, comprising of  $p^2$  blocks of  $N \times N$  matrices  $\mathcal{H}_{qq'}$ , defined as

$$(\mathcal{H}_{qq'})_{ij} = \frac{\partial^2}{\partial(\mathbf{w}_q)_i \, \partial(\mathbf{w}_{q'})_j} \sum_{\mu=1}^{\alpha N} \ell(\{u_l^{\mu}\}, \{\lambda_k^{\mu}\}, \{\mathbf{x}^{\mu}\}) \equiv \sum_{\mu=1}^{\alpha N} F_{qq'}^{\mu} x_i^{\mu} x_j^{\mu}, \tag{4}$$

where 
$$F_{qq'}^{\mu} = \frac{2}{p} \cdot \frac{\frac{2}{p} \lambda_q^{\mu} \lambda_{q'}^{\mu} + \delta_{qq'} \left[ \frac{1}{p} \sum_{k=1}^{p} (\lambda_k^{\mu})^2 - \frac{1}{p^*} \sum_{l=1}^{p^*} (u_l^{\mu})^2 \right]}{a + \frac{1}{p^*} \sum_{l=1}^{p^*} (u_l^{\mu})^2},$$
 (5)

when the pre-activations  $\{\lambda_k^{\mu}\}$  and  $\{u_l^{\mu}\}$  are random iid variables  $\mathcal{N}(0,1)$ .

Let  $\{h_i\}$  denote the eigenvalues of  $\mathcal{H}$ . In the large-N limit, the spectrum consists of a continuous "bulk" component, described by the density

$$\rho(\lambda) = \lim_{N \to \infty} \frac{1}{pN} \sum_{i=1}^{pN} \delta(\lambda - h_i), \tag{6}$$

along with a finite number of outlier eigenvalues. From these, one can extract information about the geometry of the loss landscape, such as the presence of directions correlated with the signal. This procedure can be connected to a broader class of techniques known as *spectral methods* (Lu & Li, 2020; Mondelli & Montanari, 2018; Maillard et al., 2022). These approaches are based on constructing matrices of the form

$$\mathcal{D} = \sum_{i=1}^{\alpha N} T(y(\mathbf{x}^{\mu})) \mathbf{x}^{\mu} (\mathbf{x}^{\mu})^{T},$$
 (7)

where  $T:\mathbb{R}\to\mathbb{R}$  is an appropriate pre-processing function, to study the simple phase retrieval problem (which in our notation corresponds to the  $p=p^*=1$  case). The leading eigenvector, *i.e.* the eigenvector associated with the largest or smallest eigenvalue, depending on the sign convention, is then computed to provide an estimate of the underlying signal. This estimate can be used directly as a proxy for the signal or serve as an initialization for a subsequent descent-like optimization algorithm.

Whether this spectral reconstruction successfully aligns with the true signal depends on the signal-to-noise ratio  $\alpha$ . This phenomenon is captured by the Baik–Ben Arous–Péché (BBP) transition (Baik et al., 2005), which describes a phase boundary in the spectrum: only when the signal-to-noise ratio exceeds a critical threshold  $\alpha_{BBP}$  does a leading eigenvalue detach from the bulk of the spectrum, allowing its associated eigenvector to carry non-trivial information about the signal. Below this threshold, the spectrum remains uninformative, and the leading eigenvector fails to align with the teacher.

Interestingly, for  $p=p^*=1$  the forms of matrices  $\mathcal H$  and  $\mathcal D$  are similar, the main difference being that the pre-processing function T only depends on the labels  $y(\mathbf x^\mu)$  while the factors  $F_{11}^\mu$  depend both on the labels and the student outputs  $\hat y(\mathbf x^\mu)$ . For the right function T however,  $\mathcal H$  can be mapped into  $\mathcal D$  by averaging over the student weights  $\mathbf w$ . Spectral methods then can be interpreted as extracting information from this averaged Hessian. This was first noted in Biroli et al. (2020), where authors use this perspective to develop a spectral method for a different inference problem called tensor PCA.

In this work, rather than studying the averaged Hessian, we study the spectral properties of the actual Hessian, following the lines of Bonnaire et al. (2024). We extend this analysis to the more general case of arbitrary student and teacher widths  $(p, p^*)$ . Specifically, in this work we study the BBP transition of the training loss Hessian at initialization, i.e., when the student network weights are randomly and independently sampled from the sphere  $S_{N-1}(\sqrt{N})$ , for a teacher with a generic number of nodes  $(p^* \geq 1)$ , and examine the effect of student overparameterization  $(p > p^*)$ . In some sense, overparameterization can be viewed as implicitly averaging the loss landscape across the many student nodes. Indeed, we will show that in the limit of infinite overparameterization, the performance converges to that of the optimal spectral method found in Mondelli & Montanari (2018) for  $p^* = 1$ .

To build intuition for how the BBP transition extends beyond the phase retrieval setting, we begin by recalling the simpler case. In phase retrieval, for signal-to-noise ratios larger than a critical threshold  $\alpha_{BBP}$  a single eigenvalue  $\lambda^*$  separates from the bulk of the spectrum, and its associated eigenvector  $\mathbf{v}^*$  exhibits nontrivial alignment with the signal vector  $\mathbf{v}$ . This alignment is quantified by the normalized overlap

$$m = \frac{\mathbf{v}^* \cdot \mathbf{v}}{\|\mathbf{v}^*\| \|\mathbf{v}\|}.$$
 (8)

In the more general two-layer teacher setting, isolated eigenvalues similarly correspond to alignments between student and teacher nodes. The student output can be rewritten as

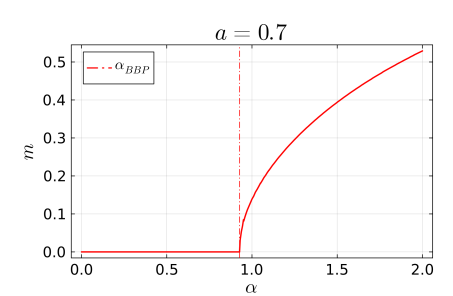
$$\hat{y}(\mathbf{x}^{\mu}) = (\mathbf{x}^{\mu})^{\top} \frac{\mathbf{W}^{\top} \mathbf{W}}{p} \mathbf{x}^{\mu}; \quad \mathbf{W} \in \mathbb{R}^{p \times N}, \ W_{ki} = (\mathbf{w}_k)_i,$$
(9)

where the matrix  $\mathbf{W}$  collects the student weight vectors  $\mathbf{w}_k$ . This expression is invariant under rotations  $\mathbf{W} \mapsto \mathbf{O}\mathbf{W}$  with  $\mathbf{O} \in \mathbb{R}^{p \times p}$  an orthogonal matrix, implying that the learned configuration is only identifiable up to orthogonal transformations (Sarao Mannelli et al., 2020b; Martin et al., 2024; Bocchi et al., 2025b). As a consequence, all student—teacher overlaps are equivalent and, also in this case, can be summarized by a single scalar parameter m. Further details can be found in appendix C.

# 3 RESULTS

In this section we present the main analytical predictions for the BBP thresholds and their comparison with finite-N simulations. All derivations, including the field theory techniques used to compute the bulk distribution and outlier eigenvalue, are deferred to the Appendices A and B.

#### 3.1 ANALYTICAL BBP TRANSITION



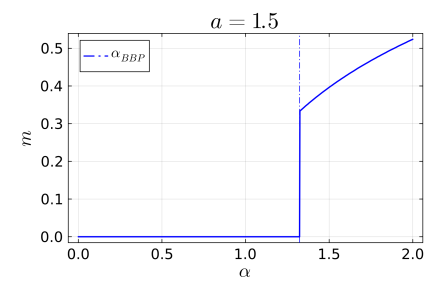


Figure 1: Overlap between the signal estimate and the true signal as a function of  $\alpha$  for continuous BBP (*Left*) and discontinuous BBP (*Right*), with p = 2 and  $p^* = 1$ .

The critical value  $\alpha_{\rm BBP}$  is analytically determined by imposing the condition

$$\lambda_*(\alpha_{BBP}) = \lambda_-(\alpha_{BBP}),\tag{10}$$

where  $\lambda_-$  denotes the left edge of the bulk spectrum and  $\lambda_*$  denotes the outlier eigenvalue. Depending on how the eigenvalue spectrum  $\rho(\lambda)$  vanishes near its left edge when equation 10 is satisfied, the nature of the BBP transition can be one of two types, either **continuous** or **discontinuous** (Bocchi et al., 2025a; Bouchbinder et al., 2021; Potters & Bouchaud, 2020). A more detailed analysis of discontinuous BBP transitions and their finite size effects is addressed in Bocchi et al. (2025a). For the sake of completeness here we re-discuss some aspects in relation to their application to our teacher-student learning problem.

In the continuous BBP transition, the overlap m between the eigenvector associated with the outlier eigenvalue and the signal(s) continuously grows from 0 to finite values as the signal-to-noise ratio  $\alpha$  increases above the threshold  $\alpha_{BBP}$ . This case corresponds to a *sharp* edge of the spectrum, where the eigenvalue density vanishes with a square-root singularity:

$$\rho(\lambda) \underset{\lambda \to \lambda^{sh}}{\propto} (\lambda - \lambda_{-}^{sh})^{1/2}. \tag{11}$$

In contrast, if the BBP transition is discontinuous the value of the overlap immediately jumps from 0 to a finite value as soon as  $\alpha > \alpha_{BBP}$ . This occurs when the left edge of the spectrum is *smooth*, with the density decaying exponentially as

$$\rho(\lambda) \underset{\lambda \to \lambda_{-}^{sm}}{\propto} \exp\left[-\frac{A}{(\lambda - \lambda_{-}^{sm})}\right], \quad \text{for some constant } A > 0.$$
 (12)

In Figure 1 we show the behavior of the overlap in the two different scenarios. While their difference is clear in the large dimensional limit  $N \to \infty$ , a distinction between the two types of transitions is also visible for finite system sizes, as discontinuous BBP transitions are characterized by a strong anticipation of the transition at N finite, which we discuss in Section 3.2.

Depending on the student and teacher number of nodes p,  $p^*$ , as well as the normalizing constant a, either type of transition can occur. In what follows, we present results for  $p^*=1$ , but we verify in the appendix D that varying  $p^*$  does not qualitatively alter the overall picture. Figure 2 shows the critical ratio  $\alpha_{\rm BBP}$ , revealing two principal effects. First,  $\alpha_{\rm BBP}(a)$  shows non-monotonic dependence on a at fixed p, with its minimum placed at a critical value  $a_c(p)$  where the transition changes from continuous (left) to discontinuous (right). In other words, for given p (and  $p^*$ ), the most convenient a allowing for an earliest recovery transition is the one where the BBP transition is at the verge of

becoming discontinuous. Second, while increasing p at fixed a generally reduces  $\alpha_{\rm BBP}$ , we again observe a critical threshold  $p_c(a)$  beyond which the transition becomes discontinuous. Note that in its vicinity (see middle inset of Figure 2) a non-monotonic  $\alpha_{\rm BBP}(p)$  behavior is sometimes visible: the subsequent small increase of  $\alpha_{\rm BBP}(p)$  with p, i.e. increasing overparametrization, is at odds with the general expectation of the benefits of overparametrization in smoothening the landscape to let the signal emerge. However, as we will see in Section 3.2, this weak effect obtained in the infinite dimensional limit can be masked by strong, non-trivial finite-size effects, reinstating a general advantage of overparametrization for all practical purposes.

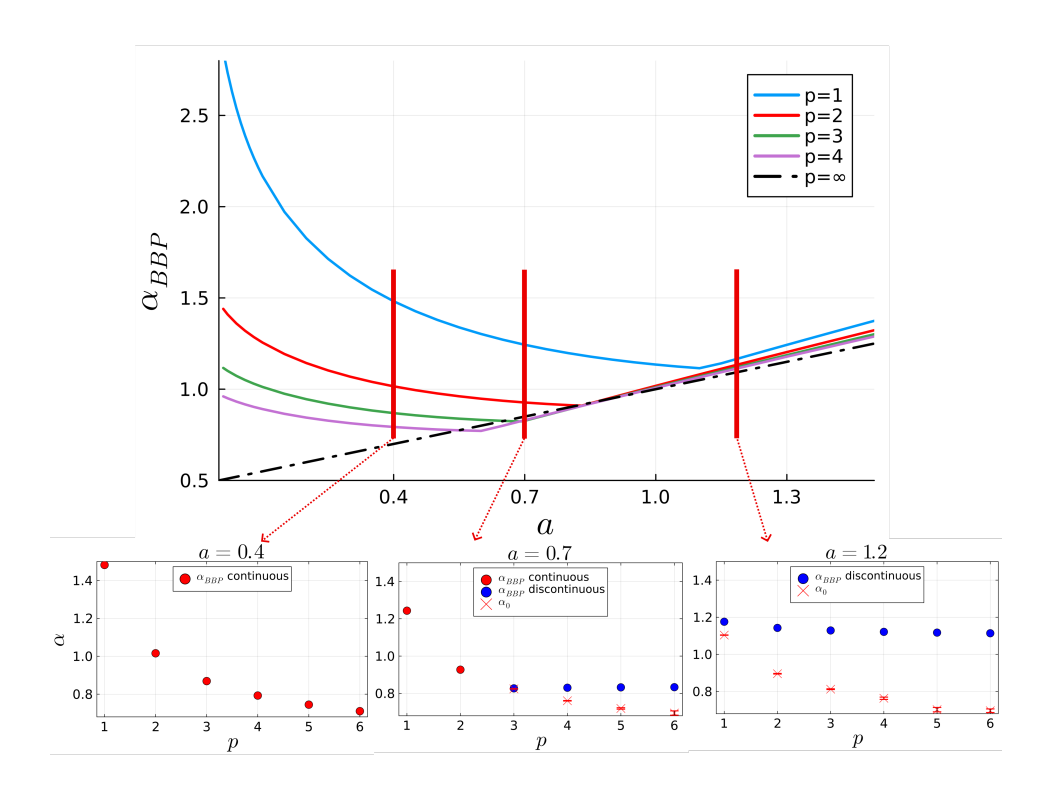


Figure 2:  $\alpha_{BBP}$  as a function of a for  $p^*=1$  and several values of p. The point at which the curves start increasing almost linearly is the point in which the transition becomes discontinuous. The dashed line shows  $\alpha_{BBP}(a)$  in the large overparametrization limit where the transition is always discontinuous. The insets show  $\alpha_{BBP}$  as a function of p for three fixed values of a. Here, red points indicate the transition is continuous, while blue points that it is discontinuous. The red crosses are estimates of  $\alpha_0$ , a "finite-N" estimate of the transition described in section 3.2.

Infinite overparametrization limit Before analyzing finite-size effects, we consider the limit of infinite overparametrization,  $p \to \infty$ . This limit is taken after the  $N \to \infty$  limit, so we remain in the regime where  $p \ll N$ . In appendix B we show that in this limit the BBP transition is always discontinuous, with a threshold given by

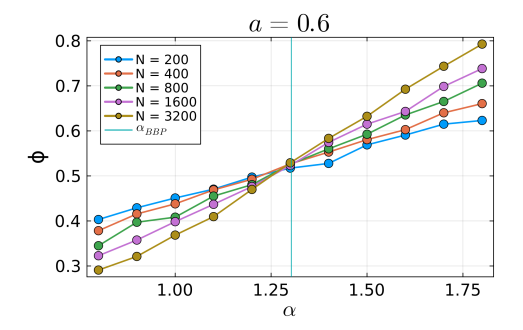
$$\alpha_{\text{BBP}}^{p=\infty} = \frac{p^*(a+1)}{2}.\tag{13}$$

For any value of  $p^*$ , the minimum of  $\alpha_{\rm BBP}^{p=\infty}$  occurs at a=0 and is equal to  $p^*/2$ , matching the information-theoretic weak recovery threshold identified in Maillard et al. (2024). Note that our setting is far from being Bayes optimal as in Maillard et al. (2024) since the overparametrized student, by definition, does not match the teacher structure. Yet, this result shows how powerful overparametrization can be, as in the large overparametrization limit, even simply extracting spectral

information from the Hessian at random configurations, the optimal weak recovery threshold can be achieved.

#### 3.2 Numerical Simulations and Finite N BBP Transition

In this section we compare the BBP thresholds calculated above with the empirical BBP threshold obtained in simulations of finite-dimensional problems with  $p=p^*=1$ . For a fixed value of a, and over a range of values of  $\alpha$ , we generate the Hessian  ${\cal H}$  for several values of the dimensionality N of the problem, look at its eigenvalue spectrum, and count the number of times the eigenvalue associated to the eigenvector with maximum overlap with the signal is the smallest. In theory, this frequency, which we denote with the letter  $\phi$ , should go from 0 to 1 discontinuously in the  $N \to \infty$  limit at  $\alpha_{BBP}$ . We perform this experiment for values of a for which the transition is both continuous and discontinuous.



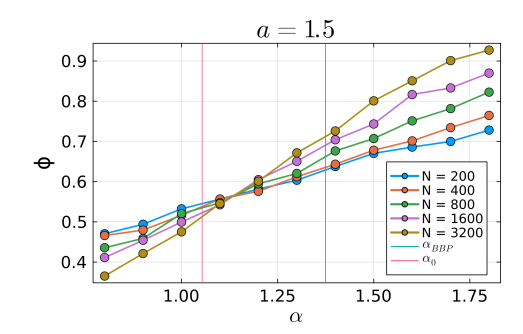


Figure 3: Comparison of BBP transitions for  $p=p^*=1$ . On the y axis we plot  $\phi$ , defined as the fraction of times the eigenvector with the maximum overlap with the signal corresponds to the smallest eigenvalue. On the left a value of a for which the transition is continuous, on the right a value for which it is discontinuous. The vertical blue lines show our prediction for the BBP threshold, while for the discontinuous case the red line shows our estimate of  $\alpha_0$ .

We observe that when the transition is continuous, the predicted  $\alpha_{BBP}$  threshold matches the point in which the curves for different values of N intersect, while when it is discontinuous the threshold evaluated in the large N-limit is always above this point. That is, in the discontinuous case, our  $N \to \infty$  prediction for  $\alpha_{BBP}$  greatly overestimates the finite N behavior. The explanation of this phenomenon is related to the shape of  $\rho(\lambda)$  near the edge. When the transition is continuous the left edge is *sharp* and for a finite N matrix then the typical deviation of the smallest eigenvalue of the bulk from the left edge is of the order of  $N^{-2/3}$ . When the BBP transition is discontinuous the left edge is *smooth* and, as a consequence, for a finite N matrix it is much harder to sample this tail of the eigenvalue distribution and the smallest eigenvalue of the bulk will be larger than the  $N \to \infty$ edge by a distance of the order of  $1/\log(N) \gg N^{-2/3}$  (Bocchi et al., 2025a). Therefore the tails of the eigenvalue distributions for finite dimensional problems are much shorter than expected and allow the BBP eigenvalue to exit the bulk earlier. Unlike continuous BBP transitions, here the BBP eigenvalue retains a finite amount of information about the signal at the transition point and continues to do so for  $\alpha < \alpha_{BBP}$ , at least long as it remains the smallest eigenvalue of the finite-N matrices. These strong finite-size effects and the residual information explain why the observed algorithmic threshold (Figure 3, right panel) lies below the predicted  $\alpha_{BBP}$  in the discontinuous case. To corroborate this explanation we conjecture that the residual information m about the teacher carried by the BBP eigenvalue for  $\alpha < \alpha_{BBP}$  must decrease following a square root behavior until its vanishing at a smaller  $\alpha_0$ . Calculating the values of  $m^2$  for various values of  $\alpha > \alpha_{BBP}$ , it is possible to perform a linear fit and obtain  $\alpha_0$  from the intersection with the x axis. The result of this analysis is shown in Figure 4. The inset shows how the value of the threshold is extracted. On the right side of the plot we see the predicted discontinuous BBP transition as a function of a for a couple of p and  $p^* = 1$  and the extrapolated signal to noise ratio  $\alpha_0$  at which it is expected that the BBP eigenvalue will completely loose its information about the teacher. As we can see, this threshold lies below the corresponding predicted discontinuous BBP transition and slightly below

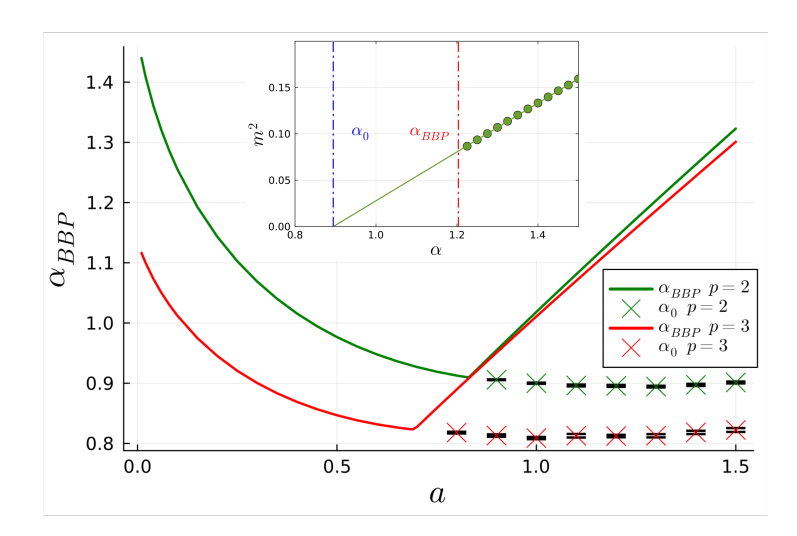


Figure 4:  $\alpha_{BBP}$  (solid) and  $\alpha_0$  (crosses) for two different values of p as a function of a.

the empirical transition for the finite dimensional version of the problem as shown in the right panel of Figure 3. The expectation is that  $\alpha_0$  must represent a lower bound for the empirical transition at finite N described above and that the empirical transition will very slowly move to the higher  $\alpha$  as N increases as the bulk eigenvalues will populate the tail progressively hiding the BBP eigenvalue.

We also reported the estimated threshold  $\alpha_0$  for the loss of information in the BBP eigenvalue in the middle and left insets of Figure 2. Note that it appears to always monotonically decrease with p, finally supporting the intuitive principle that overparametrization should favor learning.

## 4 CONCLUSION AND DISCUSSION

In this work, we presented a theoretical analysis of the loss landscape at initialization for a teacherstudent setup with quadratic activation, considering networks with a generic, but finite, number of nodes, both for the teacher and the student. We investigated whether it is possible to extract information about the teacher simply by looking at the spectral properties of the Hessian at initialization, which reflects the curvature of the loss landscape in random configurations, without using iterative algorithms like gradient descent. In the high-dimensional data limit where both the input dimension N and dataset size M diverge while maintaining a finite signal-to-noise ratio  $\alpha = M/N \sim O(1)$ , we obtain that at small  $\alpha$  the initial Hessian contains no information about the teacher, while at larger  $\alpha$  one or more Hessian's principal eigenvectors develop a finite correlation with the teacher in a phenomenon called BBP transition. This approach resembles that of spectral algorithms (Mondelli & Montanari, 2018), which employ matrices that for some inference problems can be seen (Biroli et al., 2020) as Hessians averaged over many random choices of the student weights, to recover signals via spectral analysis. Nevertheless, our approach makes it possible to isolate the effect of overparametrization on this signal recovery transition. We complemented our theoretical findings with numerical simulations, fully characterizing this phenomenon for both finite and infinite N. Our analysis leads to the following key results:

The BBP transition varies qualitatively with overparameterization and choice of loss. Depending on the number of student nodes p and the loss function's normalization constant a, the transition can be either continuous or discontinuous. The key difference between the two cases lies in the overlap behavior at the transition: in the continuous case, the correlation with the teacher increases smoothly from zero when  $\alpha$  increases, while in the discontinuous case, the outlier eigenvectors exhibit a finite overlap with the teacher immediately at the transition. Note that larger overparametrization is systematically associated to a discontinuous BBP transition for signal recovery from the spectra of the Hessian at initialization. This result comes as the first practical application of the concept of a discontinuous BBP transition—very recently introduced and discussed in Potters

433

434 435

436

437

438

439

440

441

442

443

444

445 446

447

448

449

450

451

452

453

454

455

456

457

458

459

460

461

462

463 464 465

466

467

468

469

471

472

473

474

475

476

477

478

479

480 481

482

483

484

485

& Bouchaud (2020); Bocchi et al. (2025a)-in association with overparametrization for a machine learning problem.

Overparameterization tends to anticipate the transition, with notable exceptions. Increasing p (i.e., overparameterizing the student) for fixed a generally lowers  $\alpha_{\rm BBP}$ , so that larger networks need less data to develop informative modes. Yet, for each fixed normalizing constant a, there exists a critical student size  $p_c(a)$  beyond which the transition becomes discontinuous. Near this threshold,  $\alpha_{\rm BBP}(p)$  can be non-monotonic and its precise shape depends on a. On the one hand, the overall trend confirms the generally established intuition that overparametrization is beneficial to learning, even extending it to the possibility to retrieve information about the teacher at initialization. On the other hand we observe notable, despite of small entity, exceptions to such behaviour. Surprisingly the entity of such exceptions ends up being further mitigated by finite size correction in empirical observations, reinstating a general advantage of overparametrization for most practical purposes.

The large overparametrization limit achieves optimal performances. In the limit of infinite overparameterization  $(p \to \infty)$  the information about the teacher appears through a discontinuous transition for all values of a. The large overparametrization limit could be intuitively understood as having a student able to reproduce the teacher's choice of weights an infinite number of times. This aspect has been already discussed in other contexts (Biroli et al., 2020) to highlight how largely overparametrized students can avoid overfitting and reach better generalization results as if they had access to a sort of average information of the loss landscape. For the learning problem discussed here, the spectral study of the averaged curvature of the loss landscape at initialization corresponds to preexistent spectral initialization methods (Mondelli & Montanari, 2018). In particular, signal recovery from such spectral analysis has been studied in Bocchi et al. (2025a), and it does not quantitatively match the BBP transition in the large overparametrization limit, since the former requires a stronger signal-to-noise ratio. Finally, for  $a \to 0$ , the BBP threshold  $\alpha_{\rm BBP}$  obtained in the large overparametrization limit converges to the information-theoretic transition for weak recovery. This last observation is particularly surprising and highlights how powerful overparametrization can be in deforming the loss landscape so to favor the emergence of the hidden signal. Simple spectral analysis of the Hessian at initialization in the large overparametrization limit, and therefore far from the Bayes optimal settings, is indeed enough to match the weak recovery threshold in optimal conditions.

Finite-size correction affects the discontinuous BBP transition. We compared the predictions for the BBP transition at different values of p,  $p^*$ , and a with its numerical estimation for problems with finite-dimensional datasets, for several value of the dimensionality N. We obtained very good agreement in the case of continuous BBP transition but we observed a strong mismatch in the case of discontinuous BBP transitions. As also discussed in general in Bocchi et al. (2025a), we argued that these effects must be very strong-logarithmic in N. They are due to the smooth nature of the spectral edge, which finite-N matrices fail to properly sample, and the large amount of residual information of the leading eigenvector even below the transition point. The undersampling of the tails gets stronger the lower N and it allows the BBP eigenvalue to emerge earlier than the predicted BBP threshold, resulting in a numerical signal-recovery transition much lower than the predicted BBP transition. We also extract a lower bound  $\alpha_0$  to the numerical transition evaluating the signalto-noise ratio where the extrapolated overlap of the leading eigenvalue vanishes as a square root. The empirical transition is expected to slowly move from  $\alpha_0$  to higher  $\alpha$  approaching the BBP transition only in the large N limit. Finally, surprisingly  $\alpha_0$  is found to decrease with p so that in the accessible finite-N cases overparametrization turns out to be effectively advantageous for the empirical signal-recovery transition even when the predicted discontinuous BBP transition gets anomalously postponed.

As suggested in Bonnaire et al. (2024), the fate of standard gradient descent should be influenced by the interplay between the emergence of the signal in the Hessian at initialization and the gradient-flow algorithmic transition. The latter can be predicted by evaluating the signal-to-noise ratio at which threshold states develop an instability toward the signal, also through a BBP transition. Understanding how overparameterization affects this second transition, both quantitatively and qualitatively, remains a very interesting open problem.

#### REFERENCES

- Gerard Ben Arous, Reza Gheissari, Jiaoyang Huang, and Aukosh Jagannath. Local geometry of high-dimensional mixture models: Effective spectral theory and dynamical transitions. *arXiv* preprint arXiv:2502.15655, 2025.
- Jinho Baik, Gérard Ben Arous, and Sandrine Péché. Phase transition of the largest eigenvalue for nonnull complex sample covariance matrices. 2005.
- Marco Baity-Jesi, Levent Sagun, Mario Geiger, Stefano Spigler, Gérard Ben Arous, Chiara Cammarota, Yann LeCun, Matthieu Wyart, and Giulio Biroli. Comparing dynamics: Deep neural networks versus glassy systems. In *International Conference on Machine Learning*, pp. 314–323. PMLR, 2018.
- Tamir Bendory, Yonina C Eldar, and Nicolas Boumal. Non-convex phase retrieval from stft measurements. *IEEE Transactions on Information Theory*, 64(1):467–484, 2017.
- Giulio Biroli, Chiara Cammarota, and Federico Ricci-Tersenghi. How to iron out rough landscapes and get optimal performances: averaged gradient descent and its application to tensor pca. *Journal of Physics A: Mathematical and Theoretical*, 53(17):174003, 2020.
- Dario Bocchi, Giulio Biroli, Chiara Cammarota, and Federico Ricci Tersenghi. Discontinuous bbp transitions. *preprint*, 2025a.
- Dario Bocchi, Theotime Regimbeau, Carlo Lucibello, Luca Saglietti, and Chiara Cammarota. Online learning for soft committee machines. *preprint*, 2025b.
- Tony Bonnaire, Giulio Biroli, and Chiara Cammarota. From zero to hero: How local curvature at artless initial conditions leads away from bad minima. *arXiv preprint arXiv:2403.02418*, 2024.
- Eran Bouchbinder, Edan Lerner, Corrado Rainone, Pierfrancesco Urbani, and Francesco Zamponi. Low-frequency vibrational spectrum of mean-field disordered systems. *Physical Review B*, 103 (17):174202, 2021.
- Pierre Bousseyroux and Marc Potters. Spectral initialization for high-dimensional phase retrieval with biased spatial directions. *arXiv preprint arXiv:2403.15548*, 2024.
- Jian-Feng Cai, Meng Huang, Dong Li, and Yang Wang. Solving phase retrieval with random initial guess is nearly as good as by spectral initialization. *Applied and Computational Harmonic Analysis*, 58:60–84, 2022.
- Yaim Cooper. Global minima of overparameterized neural networks. SIAM Journal on Mathematics of Data Science, 3(2):676–691, 2021.
- Cirano De Dominicis and Irene Giardina. *Random fields and spin glasses: a field theory approach*. Cambridge University Press, 2006.
- Yan V Fyodorov. Complexity of random energy landscapes, glass transition, and absolute value of the spectral determinant of random matrices. *Physical review letters*, 92(24):240601, 2004.
- Shengchao Liu, Dimitris Papailiopoulos, and Dimitris Achlioptas. Bad global minima exist and sgd can reach them. *Advances in Neural Information Processing Systems*, 33:8543–8552, 2020.
- Yue M Lu and Gen Li. Phase transitions of spectral initialization for high-dimensional non-convex estimation. *Information and Inference: A Journal of the IMA*, 9(3):507–541, 2020.
- Antoine Maillard, Florent Krzakala, Yue M Lu, and Lenka Zdeborová. Construction of optimal spectral methods in phase retrieval. In *Mathematical and Scientific Machine Learning*, pp. 693–720. PMLR, 2022.
- Antoine Maillard, Emanuele Troiani, Simon Martin, Florent Krzakala, and Lenka Zdeborová. Bayes-optimal learning of an extensive-width neural network from quadratically many samples. *Advances in Neural Information Processing Systems*, 37:82085–82132, 2024.

- Stefano Sarao Mannelli, Florent Krzakala, Pierfrancesco Urbani, and Lenka Zdeborova. Passed & spurious: Descent algorithms and local minima in spiked matrix-tensor models. In *international conference on machine learning*, pp. 4333–4342. PMLR, 2019.
  - Simon Martin, Francis Bach, and Giulio Biroli. On the impact of overparameterization on the training of a shallow neural network in high dimensions. In *International Conference on Artificial Intelligence and Statistics*, pp. 3655–3663. PMLR, 2024.
  - Rick P Millane. Phase retrieval in crystallography and optics. *Journal of the Optical Society of America A*, 7(3):394–411, 1990.
  - Marco Mondelli and Andrea Montanari. Fundamental limits of weak recovery with applications to phase retrieval. In *Conference On Learning Theory*, pp. 1445–1450. PMLR, 2018.
  - Andrea Montanari and Nike Sun. Spectral algorithms for tensor completion. *Communications on Pure and Applied Mathematics*, 71(11):2381–2425, 2018.
  - Praneeth Netrapalli, Prateek Jain, and Sujay Sanghavi. Phase retrieval using alternating minimization. *Advances in Neural Information Processing Systems*, 26, 2013.
  - Arkadiusz Orl, Harry Paul, et al. Phase retrieval in quantum mechanics. *Physical Review A*, 50(2): R921, 1994.
  - Marc Potters and Jean-Philippe Bouchaud. A first course in random matrix theory: for physicists, engineers and data scientists. Cambridge University Press, 2020.
  - Valentina Ros, Gerard Ben Arous, Giulio Biroli, and Chiara Cammarota. Complex energy land-scapes in spiked-tensor and simple glassy models: Ruggedness, arrangements of local minima, and phase transitions. *Physical Review X*, 9(1):011003, 2019.
  - Stefano Sarao Mannelli, Giulio Biroli, Chiara Cammarota, Florent Krzakala, and Lenka Zdeborová. Who is afraid of big bad minima? analysis of gradient-flow in spiked matrix-tensor models. *Advances in neural information processing systems*, 32, 2019.
  - Stefano Sarao Mannelli, Giulio Biroli, Chiara Cammarota, Florent Krzakala, Pierfrancesco Urbani, and Lenka Zdeborová. Complex dynamics in simple neural networks: Understanding gradient flow in phase retrieval. *Advances in Neural Information Processing Systems*, 33:3265–3274, 2020a.
  - Stefano Sarao Mannelli, Eric Vanden-Eijnden, and Lenka Zdeborová. Optimization and generalization of shallow neural networks with quadratic activation functions. *Advances in Neural Information Processing Systems*, 33:13445–13455, 2020b.
  - Alexander Shevchenko and Marco Mondelli. Landscape connectivity and dropout stability of sgd solutions for over-parameterized neural networks. In *International Conference on Machine Learning*, pp. 8773–8784. PMLR, 2020.
  - Daniel Soudry and Yair Carmon. No bad local minima: Data independent training error guarantees for multilayer neural networks. *arXiv preprint arXiv:1605.08361*, 2016.
  - Ju Sun, Qing Qu, and John Wright. A geometric analysis of phase retrieval. *Foundations of Computational Mathematics*, 18(5):1131–1198, 2018.
  - Terence Tao. Topics in random matrix theory, volume 132. American Mathematical Soc., 2012.
  - Anthony Zee. Law of addition in random matrix theory. *Nuclear Physics B*, 474(3):726–744, 1996.
    - **LLM Disclosure** LLMs were employed in this work to review the manuscript, correct grammatical errors, and polish the writing to improve clarity and readability.

## A FIELD THEORY APPROACH

In this technical section, we give an overview of a field-theoretic approach (Zee, 1996; De Dominicis & Giardina, 2006) used to derive a self-consistent equation for the Stieltjes Transform of the Hessian, defined as

$$g(z) = \lim_{N \to \infty} \mathbb{E}_{x} \frac{1}{Np} \operatorname{Tr} G(z) = \lim_{N \to \infty} \mathbb{E}_{x} \frac{1}{Np} \operatorname{Tr} \left( \frac{1}{z\mathbf{I} - \mathcal{H}} \right).$$
 (14)

The eigenvalue spectrum density can be obtained via the Stieltjes inversion formula:

$$\rho(\lambda) = \lim_{\epsilon \to 0^+} \frac{1}{\pi} \operatorname{Im} g(\lambda - i\epsilon). \tag{15}$$

Furthermore, we will build on the same formalism to obtain a self-consistent equation for the outlier eigenvalue  $\lambda^*$ , when it exists.

The first step is to use the rotational invariance of the teacher weight vectors. Without loss of generality, we fix them to lie along the first  $p^*$  canonical directions  $\boldsymbol{w}_{q_*}^* = \sqrt{N}\boldsymbol{e}_{q_*}$  for  $q_* \in \{1,\dots,p^*\}$ , where the  $\sqrt{N}$  ensures the correct normalization. With this choice, the teacher pre-activations reduce to  $u_l^\mu = \sqrt{N}x_l^\mu \sim \mathcal{N}(0,1)$ . To separate the parts of the matrix where the coefficients  $F_{qq'}$  are correlated to the components of the vectors  $\boldsymbol{x}^\mu$ , we permute the rows and columns of  $\boldsymbol{\mathcal{H}}$  so that the first  $p^*$  rows and columns of each block  $\boldsymbol{\mathcal{H}}_{qq'}$  are grouped together in the top-left corner in a submatrix with elements  $(\mathcal{H}^s)_{qq'}^{q,q'} = \sum_\mu F_{qq'}^\mu x_{q_*}^\mu x_{q_*}^\mu$  for  $q,q' \in \{1,\dots,p\}, q_*, q_*' \in \{1,\dots,p^*\}$ .  $\boldsymbol{\mathcal{H}}^s$  should be understood as a block matrix, consisting of  $(p^*)^2$  blocks, where each block is a  $p \times p$  matrix  $(\boldsymbol{\mathcal{H}}^s)^{q_*q'_*}$ . The final shape of this permuted  $\boldsymbol{\mathcal{H}}$  is

$$\mathcal{H} = \begin{pmatrix} \mathcal{H}^s & \mathcal{H}^c \\ (\mathcal{H}^c)^T & \mathcal{H}^b \end{pmatrix} \qquad \mathcal{H}^s \in \mathbb{R}^{pp^* \times pp^*}, \mathcal{H}^b \in \mathbb{R}^{(N-p^*)p \times (N-p^*)p}, \mathcal{H}^c \in \mathbb{R}^{pp^* \times (N-p^*)p}.$$
(16)

In section A.1 we calculate the spectral distribution of its bulk eigenvalues  $\rho(\lambda)$ . It is a standard Random Matrix Theory result (see for example exercise 2.4.3 of Tao (2012)) that the spectral distribution does not change if we remove a number of rows and columns whose Frobenius norm is o(N). Since every element of  $\mathcal{H}$  is O(1), the Frobenius norm of  $\mathcal{H}^s$  is clearly O(1), while by the strong law of large numbers the Frobenius norm of  $\mathcal{H}^c$  is  $O(\sqrt{N})$ . For the purpose of computing the spectrum bulk then we can simply discard them, and compute directly the Stieltjes transform of the matrix  $\mathcal{H}^b$ . We will see that this leads to a great simplification.

In section A.2 instead we focus on the  $pp^*$  outlier eigenvalues, which are not captured by the distribution  $\rho(\lambda)$ . In this case we cannot simply ignore the other blocks of the matrix  $\mathcal{H}$ . Indeed, if we divide the resolvent matrix G(z) in blocks in the same way,

$$\boldsymbol{G} = \begin{pmatrix} \tilde{\boldsymbol{G}} & \hat{\boldsymbol{G}} \\ \hat{\boldsymbol{G}}^T & \bar{\boldsymbol{G}} \end{pmatrix} \qquad \tilde{\boldsymbol{G}} \in \mathbb{R}^{pp^* \times pp^*}, \bar{\boldsymbol{G}} \in \mathbb{R}^{(N-p^*)p \times (N-p^*)p}, \hat{\boldsymbol{G}} \in \mathbb{R}^{pp^* \times (N-p^*)p},$$
(17)

we have that the top left corner  $\tilde{G}$  encodes precisely for these outlier eigenvalues. Since G and  $\mathcal{H}$  are related by an inverse,  $\tilde{G}$  will depend on all four blocks of  $\mathcal{H}$ . We will calculate it exactly using field theory.

#### A.1 SPECTRUM BULK

Following Zee (1996), the starting point for the calculation of the Stieltjes transform of  $\mathcal{H}^b$  is to use a basic identity for Gaussian integration to write

$$g(z) = \lim_{N \to \infty} \mathbb{E}_{\boldsymbol{x}} \frac{1}{Np} \operatorname{Tr} \left( \frac{1}{z \boldsymbol{I}_{(N-p^*)p} - \boldsymbol{\mathcal{H}}^b} \right) =$$

$$= \lim_{N \to \infty} \mathbb{E}_{\boldsymbol{x}} \frac{1}{\mathcal{Z}} \int \prod_{q=1}^p d\boldsymbol{\psi}_q e^{-\frac{1}{2} \sum_{qq'} (\boldsymbol{\psi}_q)^T \left( z \boldsymbol{I}_{(N-p^*)p} - \boldsymbol{\mathcal{H}}^b \right)_{qq'} \boldsymbol{\psi}_{q'}} \sum_q \frac{1}{Np} \|\boldsymbol{\psi}_q\|^2.$$
(18)

Here, we introduced p  $(N-p^*)$ -dimensional scalar fields  $\psi_q$ , and denoted by  $\left(z\boldsymbol{I}-\boldsymbol{\mathcal{H}}^b\right)_{qq'}$  the qq'-th block of the matrix  $z\boldsymbol{I}-\boldsymbol{\mathcal{H}}^b$ . The next step is to get rid of the normalization constant  $\frac{1}{Z}$  using the replica trick  $\frac{1}{Z}=\lim_{n\to 0} Z^{n-1}$  and introducing n-1 replicas of the scalar fields  $\{\psi_q^a\}_{a=1}^n$ :

$$g(z) = \lim_{N \to \infty} \lim_{n \to 0} \mathbb{E}_{\boldsymbol{x}} \int \prod_{a=1}^{n} \prod_{q=1}^{p} d\psi_{q}^{a} e^{-\frac{1}{2} \sum_{aqq'} (\psi_{q}^{a})^{T} \left(z\boldsymbol{I} - \boldsymbol{\mathcal{H}}^{b}\right)_{qq'} \psi_{q'}^{a}} \sum_{q} \frac{1}{Np} \|\psi_{q}^{1}\|^{2}$$

$$\equiv \lim_{N \to \infty} \lim_{n \to 0} \left\langle \sum_{q} \frac{1}{Np} \|\psi_{q}^{1}\|^{2} \right\rangle_{n,N}.$$
(19)

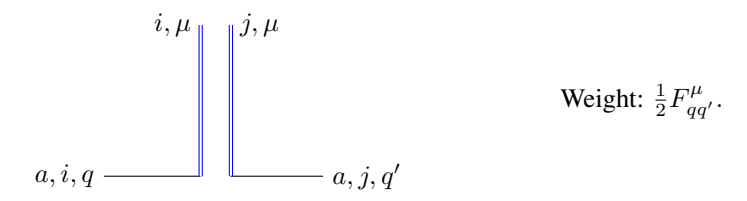
This integral cannot be performed analytically, as the  $x^{\mu}$  appear in the covariance matrix of the fields  $\psi^a_q$ . However, if we expand the exponential  $e^{-\frac{1}{2}\sum_{aqq'}(\psi^a_q)^T\mathcal{H}^b_{qq'}\psi^a_{q'}}$ , we are reduced to computing the average of every term with respect to the "bare" measure, namely the measure that appears in equation 19 with  $\mathcal{H}^b$  set to zero. Since for every element of the Hessian in the bulk

$$(\mathcal{H}_{qq'}^b)_{ij} = \sum_{\mu=1}^{\alpha N} F_{qq'}^{\mu} x_{p^*+i}^{\mu} x_{p^*+j}^{\mu}, \tag{20}$$

 $F^{\mu}_{qq'}$  is independent of  $x^{\mu}_{p^*+i}$ , we can use Wick's probability theorem–according to which every higher order moment can be expressed as a function of second moments—to compute each term of the expansion. To wield the power of Feynman diagrams we identify two fields, one for  $\psi^a_{iq}$  and one for  $x^{\mu}_i$ , which in accordance with Zee (1996) we call "quark" and "gluon" fields. Their bare propagators,  $g^0$ , are defined as the correlations of the fields in the "bare" measure. We will represent the former as straight lines and the latter as double lines.

$$a,i,q$$
  $a,i,q$   $g^0_{quark}=\frac{1}{z},$  
$$i,\mu$$
  $i,\mu$   $i,\mu$   $g^0_{qluon}=\mathbb{E}_{\mathbf{x}}x_i^2=\frac{1}{N}.$ 

The interaction between the two fields can be read off  $\mathcal{H}^b$ , and can be represented with a vertex of the following kind and its corresponding weight



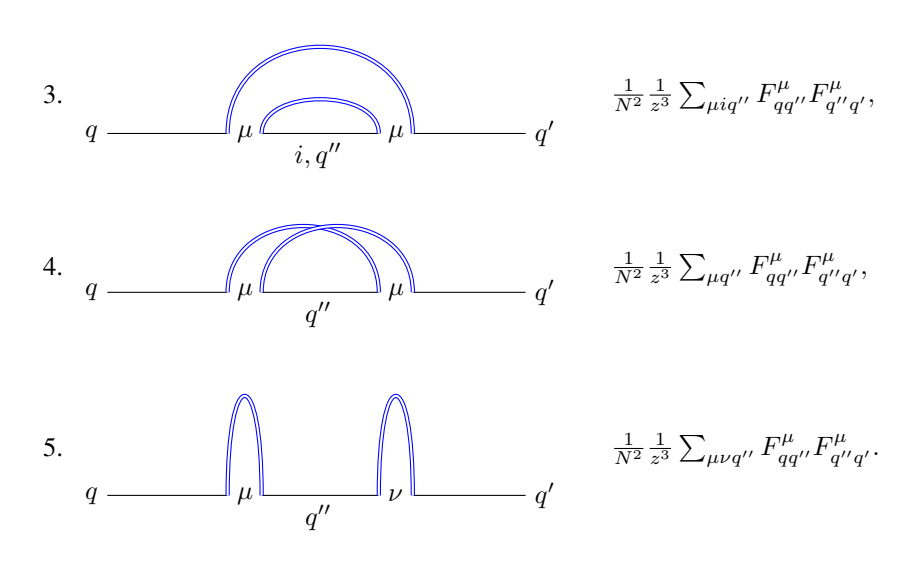
Note that although we are interested in the propagators  $\langle (\psi^1_{iq})^2 \rangle$ , to derive a self-consistent equation we will have to consider also propagators between different blocks  $\langle \psi^1_{iq} \psi^1_{iq'} \rangle$ , which don't depend on the index i. From now on we will use  $\mathbf{G}^b$  to indicate the  $p \times p$  matrix formed by these elements, and with  $\mathbf{G}^0_{quark} = g^0_{quark} \mathbf{I}_p$  the diagonal  $p \times p$  matrix that contains the bare quark propagators on the diagonal. The Stieltjes Transform can be then obtained from  $g(z) = \frac{1}{p} \mathrm{Tr} \, \mathbf{G}^b(z)$ .

Let us begin by examining the first set of diagrams. Since the contribution is identical for any index i, we may, without loss of generality, fix i=1. In the diagrams shown below, propagators associated with a, i=1 will be left unlabelled. When a propagator corresponds to a generic i or a, we will explicitly annotate it on the line as a reminder that the corresponding index must be summed over. For each diagram, we will also indicate its total weight.

With one vertex we have diagrams:

1. 
$$\frac{1}{N} \frac{1}{z^2} \sum_{\mu} F^{\mu}_{qq'},$$

Note that the total contribution of diagrams of type 2 is proportional to the number of replicas, which in the limit  $n \to 0$  goes to 0. In general, this holds for any disconnected diagram, so in the following we will focus on connected ones. Note also that in diagrams of type 1 the 1/2 factor that comes from the weight of the vertex is canceled by a factor 2 that comes from the number of ways in which the vertex can be connected. Other than this 1/2 factor, each diagram also carries an 1/n! factor, where n is the number of vertices in the diagram, from the exponential expansion in equation 19. However, this is canceled by a factor n! that comes from the number of ways the n vertices can be aligned. This cancellation happens at all orders, so we will ignore such factors from now on. Let us now consider two vertex diagrams:



The total weight of diagrams of type 4 is o(1), so their contribution is negligible in the  $N \to \infty$  limit. In general, this holds for all diagrams where gluon propagators intersect, so we will exclude these from now on.

Diagram 5 is instead obtained by connecting two diagrams of type 1 "in series". This is a general property of diagrammatic expansion: new diagrams can always be generated combining earlier ones in series through bare quark propagators. If we sum the contributions of all diagrams that are not obtained in this way, which in Quantum Field Theory are known as *one-particle irreducible* (1PI) diagrams, we can exploit this recursive structure to derive a self-consistent equation for the propagator  $G^b$ . Let us call  $\Sigma^b$  the  $p \times p$  matrix whose elements  $\Sigma^b_{qq'}$  are the sum of all such 1PI diagrams connecting fields with block indices q and q', with external bare quark propagators removed (so-called *amputated* diagrams). Then we can express the sum of all diagrams as

$$\boldsymbol{G}^{b} = \boldsymbol{G}_{quark}^{0} + \boldsymbol{G}_{quark}^{0} \boldsymbol{\Sigma}^{b} \boldsymbol{G}_{quark}^{0} + \boldsymbol{G}_{quark}^{0} \boldsymbol{\Sigma}^{b} \boldsymbol{G}_{quark}^{0} \boldsymbol{\Sigma}^{b} \boldsymbol{G}_{quark}^{0} + \dots, \tag{21}$$

Factoring out  ${\cal G}^0_{quark}$  reveals a geometric series, leading to

$$\boldsymbol{G}^{b} = \boldsymbol{G}_{quark}^{0} \left( \boldsymbol{I}_{p} + \boldsymbol{\Sigma}^{b} \boldsymbol{G}_{quark}^{0} + \boldsymbol{\Sigma}^{b} \boldsymbol{G}_{quark}^{0} \boldsymbol{\Sigma}^{b} \boldsymbol{G}_{quark}^{0} + \dots \right) = \left( (g_{quark}^{0})^{-1} \boldsymbol{I}_{p} - \boldsymbol{\Sigma}^{b} \right)^{-1}, \tag{22}$$

This gives a self-consistent equation for the matrix  $G^b$ , since  $\Sigma^b$  depends on  $G^b$ , that in Physics is known as the *Dyson* equation. This allows us to focus on 1PI diagrams from now on. Let us look at diagrams with 3 vertices.

6. 
$$q = \frac{\frac{1}{N^3} \frac{1}{z^4} \sum_{\mu i j q'' q'''} F^{\mu}_{q q''} F^{\mu}_{q'' q'''} F^{\mu}_{q''' q''}}{j, q'''} q'''$$

7. 
$$q = \frac{1}{N^3} \frac{1}{z^4} \sum_{\mu\nu ijq''q'''} F^{\mu}_{qq''} F^{\nu}_{q''q'''} F^{\mu}_{q'''q''} F^{\mu}_{q'''q''}$$

As we can see, diagrams of type 7 are just diagrams of type 3 with a diagram of type 1 added to the inner quark propagator. This is a general property that is unique to this field theory: new diagrams can be obtained from previous ones by adding them to the inner quark propagators. If the starting diagram is 1-Particle Irreducible, then so is the new diagram. Since the sum of all possible diagrams is just the propagator, this form of combination can be accounted for by substituting  $G^b_{qq'}$  to every inner bare quark line.

Indeed, the self-energy can be obtained from the sum of all leading order diagrams mentioned above, where the incoming and outgoing propagators are "amputated", and where every inner bare quark propagator is substituted by a propagator  $G_{qq'}^b$ , which we indicate graphically with a blob.

The first term in the sum is diagram of type 1, which gives a total contribution of  $\frac{1}{N}\sum_{\mu}F^{\mu}_{qq'}$ . The second term is given by diagram of type 3 with a  $G^b_{qq'}$  propagator on its inner quark line



Note that the incoming and outgoing propagators are shorter to indicate that we are considering amputated diagrams. The third term is diagram of type 6 where again we substitute propagators  $G_{qq'}$ 

$$q = \mu \bigcap_{i} \mu \bigcap_{j} \mu \bigcap_{j} \mu - q'$$
 $G^b_{a''a'''} G^b_{a'''a''''}$ 
 $G^b_{a'''a''''}$ 

Note that we do not have to consider diagram of type 7 with propagators because it is already included in the second term. The next term is just the equivalent of the previous diagram but with three inner arches, from which we can guess the general form of the diagrams that appear in the self-energy.

Summing the weights of these diagrams, we can write in matrix form

$$\Sigma^{b} = \frac{1}{N} \sum_{\mu} \mathbf{F}^{\mu} + \frac{1}{N} \sum_{\mu} \mathbf{F}^{\mu} \mathbf{G}^{b} \mathbf{F}^{\mu} + \frac{1}{N} \sum_{\mu} \mathbf{F}^{\mu} \mathbf{G}^{b} \mathbf{F}^{\mu} \mathbf{G}^{b} \mathbf{F}^{\mu} + \cdots =$$

$$= \frac{1}{N} \sum_{\mu} \mathbf{F}^{\mu} \left( \mathbf{I}_{p} + \mathbf{G}^{b} \mathbf{F}^{\mu} + \mathbf{G}^{b} \mathbf{F}^{\mu} \mathbf{G}^{b} \mathbf{F}^{\mu} + \cdots \right) = \frac{P}{N} \frac{1}{P} \sum_{\mu} \mathbf{F}^{\mu} \left( \mathbf{I}_{p} - \mathbf{G}^{b} \mathbf{F}^{\mu} \right)^{-1} \rightarrow$$

$$\rightarrow \alpha \mathbb{E} \mathbf{F} \left( \mathbf{I}_{p} - \mathbf{G}^{b} \mathbf{F} \right)^{-1}, \tag{23}$$

where in the last identity we assumed that in the  $N \to \infty$  the sum concentrates to its mean with respect to the dataset distribution.

Plugging this expression into equation 22, we get that the propagator satisfies the self-consistent equation

$$(\mathbf{G}^b)^{-1} = z\mathbf{I}_p - \alpha \mathbb{E}\mathbf{F} \left(\mathbf{I}_p - \mathbf{G}^b \mathbf{F}\right)^{-1}.$$
 (24)

Note that the F matrix is of the form  $F = \alpha \lambda \lambda^T + \beta I_p$  where  $\lambda$  is a standard Gaussian vector. In particular, it is rotationally invariant, so this equation should hold also for  $O^T FO$  where O is a rotation matrix.

$$(\mathbf{G}^b)^{-1} = z\mathbf{I}_p - \alpha \mathbb{E}\mathbf{O}^T \mathbf{F}\mathbf{O} \left(\mathbf{I}_p - \mathbf{G}^b \mathbf{O}^T \mathbf{F}\mathbf{O}\right)^{-1}, \tag{25}$$

from which

$$(\mathbf{O}\mathbf{G}^b\mathbf{O}^T)^{-1} = z\mathbf{I}_p - \alpha \mathbb{E}\mathbf{F} \left(\mathbf{I}_p - \mathbf{O}\mathbf{G}^b\mathbf{O}^T\mathbf{F}\right)^{-1}.$$
 (26)

This must hold for any rotation matrix O, so this implies that the matrix G must be proportional to the identity matrix. If we call g(z) the value on the diagonal, equation 24 can be written in scalar form

$$g^{-1}(z) = z - \alpha \frac{1}{p} \sum_{l=1}^{p} \mathbb{E} \operatorname{Tr} \left[ \boldsymbol{F} \left( \boldsymbol{I}_{p} - g(z) \boldsymbol{F} \right)^{-1} \right] = z - \alpha \frac{1}{p} \sum_{l=1}^{p} \mathbb{E} \left[ \frac{c_{l}}{1 - g(z)c_{l}} \right], \quad (27)$$

where the  $c_l$  are the eigenvalues of the F matrix.

#### A.2 OUTLIER EIGENVALUE

The starting point for the calculation of the outlier eigenvalues is similar, with the exception that we have to consider the full matrix  $\mathcal{H}$  to calculate the elements of  $\tilde{G}(z)$ :

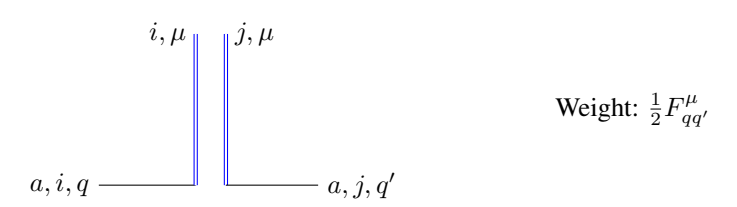
$$\tilde{G}_{qq'}^{q_*q_*'}(z) = \lim_{n \to 0} \mathbb{E}_{\boldsymbol{x}} \int \prod_{a=1}^n \prod_{q=1}^p d\psi_q^a e^{-\frac{1}{2} \sum_a (\psi^a)_<^T \left( z \boldsymbol{I}_{pp^*} - \mathcal{H}^s \right) (\psi^a)_< + \sum_a (\psi^a)_<^T \mathcal{H}^c(\psi^a)_>} \times \\
\times e^{-\frac{1}{2} \sum_a (\psi^a)_>^T \left( z \boldsymbol{I}_{p(N-p^*)} - \mathcal{H}^b \right) (\psi^a)_>} \psi_{q_*q}^1 \psi_{q_*'q'}^1. \tag{28}$$

Here, we introduce the notation  $(\psi^a)_<$  to denote for each a the  $pp^*$ -dimensional vector with components  $\psi^a_{iq}$  for  $q \in \{1,\dots,p\}, i \in \{1,\dots,p^*\}$ , and similarly  $(\psi^a)_>$  the  $p(N-p^*)$ -dimensional vector of components  $\psi^a_{iq}$  for  $q \in \{1,\dots,p\}, i \in \{p^*+1,\dots,N\}$ . The vectors are flattened in a way that the first p components of  $(\psi^a)_<$  and  $(\psi^a)_>$  are respectively  $\{\psi^a_{1q}\}_{q=1}^p$  and  $\{\psi^a_{(p^*+1)q}\}_{q=1}^p$ , the second p components are  $\{\psi^a_{2q}\}_{q=1}^p$  and  $\{\psi^a_{(p^*+2)q}\}_{q=1}^p$  and so on.

As before, we can calculate this integral using diagrammatic expansion, with the only difference that we cannot average over the first  $p^*$  components of the  $\boldsymbol{x}^{\mu}$  field, since they appear in  $F^{\mu}_{qq'}$  and we cannot simply use Wick's probability theorem. Indicating this time by a curly line the bare propagator between fields with indexes that belong to  $(\psi^a)_{<}$ , and with straight lines indexes belonging to  $(\psi^a)_{>}$ , we have that the bare propagators are

$$\begin{array}{ll} q,q_* & \qquad \qquad \tilde{g}^0 = \frac{1}{z - \frac{1}{N} \sum_{\mu} F_{qq}^{\mu}(u_{q_*}^{\mu})^2} \rightarrow \frac{1}{z - \alpha \mathbb{E} F_{qq} u_{q_*}^2} \\ \\ a,i,q & \qquad \qquad a,i,q & \qquad \qquad g_{quark}^0 = \frac{1}{z} \\ \\ i,\mu & \qquad \qquad i,\mu & \qquad \qquad g_{gluon}^0 = \frac{1}{N} \end{array}$$

The vertices are instead given by the old one



and a new one

$$\begin{array}{c|c} i,q \\ \hline \\ i,q \\ \hline \\ \downarrow \\ \iota,q \\ \hline \end{array}$$
 Weight:  $\frac{1}{\sqrt{N}}F^{\mu}_{qq'}u^{\mu}_{q_*}$ 

As before, let us define the self-energy  $\tilde{\Sigma}_{qq'}^{q_*q'_*}$  as the sum of all 1PI diagrams connecting the curly fields with indices  $q,q_*$  and  $q',q'_*$ . Again interpreting  $\tilde{\Sigma}$  as a block matrix, with  $(p^*)^2$  blocks of  $p \times p$ -dimensional matrices  $\tilde{\Sigma}^{q_*q'_*}$ , then we can write a matrix Dyson equation for the resolvent

$$\tilde{\boldsymbol{G}} = \left( (\tilde{g}^0)^{-1} \boldsymbol{I}_{pp^*} - \tilde{\boldsymbol{\Sigma}} \right)^{-1}. \tag{29}$$

We expect the matrix  $\tilde{G}$  to be singular when z is equal to the outlier eigenvalue, so a self-consistent equation can be obtained by imposing the singularity of  $(\tilde{g}^0)^{-1}I_p - \tilde{\Sigma}$ .

Let us now calculate the self-energy directly, using the same rules we found above, namely that disconnected and gluon-intersected diagrams are subleading. As we are looking for the self-energy of the "curly" field, we will necessarily need two vertices of the second kind. The first term is given precisely by two such vertices

1. 
$$q, q_* \sim \mu \underbrace{\sum_{i} \mu \sim q', q'_*}_{i}$$
 
$$\underbrace{\frac{1}{N^2} \sum_{\mu i} \left( \mathbf{F}^{\mu} \mathbf{G}^{b} \mathbf{F}^{\mu} \right)_{qq'} u^{\mu}_{q_*} u^{\mu}_{q'_*}}_{q'_*}$$

Next, we can add a vertex of the first kind to get the diagrams

2. 
$$q, q_* \sim \mu \underbrace{\sum_{i=1}^{b} \mu_{j}}_{j} \mu \sim q', q'_* \qquad \frac{1}{N^3} \sum_{\mu ij} \left( \mathbf{F}^{\mu} \mathbf{G}^{b} \mathbf{F}^{\mu} \mathbf{G}^{b} \mathbf{F}^{\mu} \right)_{qq'} u^{\mu}_{q_*} u^{\mu}_{q'_*}$$

3. 
$$q, q_* \sim \mu \underbrace{i}_{i} \underbrace{\nu}_{i} \underbrace{\nu}_{i} \underbrace{\mu}_{i} \sim q', q'_*$$
 
$$\underbrace{\frac{1}{N^3} \sum_{\mu\nu i} \left( \mathbf{F}^{\mu} \mathbf{G}^{b} \mathbf{F}^{\nu} \mathbf{G}^{b} \mathbf{F}^{\mu} \right)_{qq'}}_{q_* u_{q_*}^{\mu} u_{q'_*}^{\mu}}$$

Diagrams of type 3 however are already counted in diagrams of type 1. We could also add two vertices of the second kind, but we would not obtain 1PI diagrams.

The next diagram is obtained by stacking one more arch to diagram 2, and again we can guess the iterative form of the diagrams that contribute. Summing the weight of all such diagrams, and remembering that  $G^b = g(z)I_p$ , we get that the self-energy is

$$\tilde{\boldsymbol{\Sigma}}^{q_*q'_*} = \frac{1}{N} \sum_{\mu} u^{\mu}_{q_*} u^{\mu}_{q'_*} \left( g(z) \boldsymbol{F}^{\mu} \boldsymbol{F}^{\mu} + g^2(z) \boldsymbol{F}^{\mu} \boldsymbol{F}^{\mu} \boldsymbol{F}^{\mu} + \dots \right) = \\
= \frac{1}{N} \sum_{\mu} u^{\mu}_{q_*} u^{\mu}_{q'_*} \left[ g(z) \left( \boldsymbol{F}^{\mu} \right)^2 \left( \boldsymbol{I}_p - \boldsymbol{F}^{\mu} g(z) \right)^{-1} \right] \rightarrow \alpha \mathbb{E} u_{q_*} u_{q'_*} \left[ g(z) \boldsymbol{F}^2 \left( \boldsymbol{I}_p - \boldsymbol{F} g(z) \right)^{-1} \right],$$
(30)

where again in the last equation we supposed that the sum concentrates to its mean with respect to the dataset. Since F is an even function of  $u_{q_*}$ ,  $\tilde{\Sigma}_{qq'}^{q_*q_*'}$  is 0 for  $q_* \neq q_*'$  (and in particular, the expectation will be the same for every index  $q_*$ ). Using the fact that  $G^b$  is diagonal we can write

$$\tilde{\boldsymbol{\Sigma}}^{q_*q_*} = \alpha \mathbb{E}u_{q_*}^2 \left[ g(z) \boldsymbol{F}^2 \left( \boldsymbol{I}_p - \boldsymbol{F}g(z) \right)^{-1} \right]$$
(31)

Again, F is rotationally invariant, so the same equation should hold for a rotated F

$$\tilde{\boldsymbol{\Sigma}}^{q_*q_*} = \alpha \mathbb{E}u_{q_*}^2 \left[ g(z) \boldsymbol{O}^T \boldsymbol{F}^2 \boldsymbol{O} \left( \boldsymbol{I}_p - \boldsymbol{O}^T \boldsymbol{F} \boldsymbol{O} g(z) \right)^{-1} \right]$$
(32)

from which

$$O\tilde{\Sigma}^{q_*q_*}O^T = \alpha \mathbb{E}u_{q_*}^2 \left[ g(z) F^2 \left( I_p - Fg(z) \right)^{-1} \right]$$
(33)

For this equation to hold for every rotation matrix O, the matrix  $\tilde{\Sigma}^{q_*q_*}$  must be proportional to the identity. Consequently, we obtain  $\tilde{\Sigma}_{qq'}^{q_*q_*} = \tilde{\Sigma}(z)\delta_{qq'}\delta_{q_*q'_*}$ . Imposing the singularity of the RHS of equation 29, we get the equation

$$\left(\lambda^* - \alpha \mathbb{E} F_{11} u_1^2 - \tilde{\Sigma}(\lambda^*)\right)^{pp^*} = 0. \tag{34}$$

In other words, the  $pp^*$  outliers all coincide with a value  $\lambda^*$  which can be found by solving the self-consistent equation

$$\lambda^* = \alpha \mathbb{E} u_1^2 \frac{1}{p} \text{Tr} \Big[ \mathbf{F} \Big( 1 + g(\lambda^*) \mathbf{F} \Big( \mathbf{I}_p - \mathbf{F} g(\lambda^*) \Big)^{-1} \Big) \Big] = \alpha \frac{1}{p} \mathbb{E} u_1^2 \text{Tr} \Big[ \mathbf{F} \Big( \mathbb{I} - \mathbf{F} g(\lambda^*) \Big)^{-1} \Big]$$

$$= \alpha \mathbb{E} u_1^2 \frac{1}{p} \sum_{l=1}^p \frac{c_l}{1 - g(\lambda^*) c_l} \equiv \Xi(\lambda^*). \tag{35}$$

Combining this last expression with equation 27, one can rewrite a self-consistent equation for  $g^* \equiv g(\lambda^*)$ :

$$\frac{1}{g^*} = \alpha \mathbb{E} \left[ \frac{1}{p} \sum_{i=1}^p \frac{c_i(u_1^2 - 1)}{1 - g^* c_i} \right] . \tag{36}$$

# B ANALYTICAL COMPUTATIONS FOR THE BBP

In the large dimensional limit, in order to obtain an expression for the left edge of the spectrum bulk we define the inverse function z(q) of the resolvent q(z), using equation 27, as

$$z(g) = \frac{1}{g} + \alpha \mathbb{E} \left[ \frac{1}{p} \sum_{i=1}^{p} \frac{c_i}{1 - gc_i} \right].$$
 (37)

The density of eigenvalues  $\rho(\lambda)$  of the spectrum bulk as a function of  $z=\lambda$  will be obtained as the imaginary part of the g solution to equation 37. In particular the edges correspond to the  $z=\lambda$  where a non null imaginary part develops, which can occur by means of two different mechanisms. First: the domain of a g real is constrained by the requirement that all denominators in equation 37 do not vanish. In particular equation 37 is well-defined for  $g \in \mathbb{R} \setminus (\operatorname{supp}(1/c) \cup \{0\})$ , where  $\operatorname{supp}(1/c)$  denotes the support of 1/c across all  $c_i$ , i.e.,  $\operatorname{supp}(1/c) = \bigcup_{i=1}^p \left\{\frac{1}{x} \mid x \in \operatorname{supp}(c_i)\right\}$ . Assuming each  $c_i$  has support within  $[c_{i,\min}, c_{i,\max}]$ , we define  $c_{\min} = \min_i (c_{i,\min})$  and  $c_{\max} = \max_i (c_{i,\max})$ . If  $c_{\min} < 0$  and  $c_{\max} > 0$  (which will correspond to our case), then

$$g \in \left(\frac{1}{c_{\min}}, 0\right) \cup \left(0, \frac{1}{c_{\max}}\right) \equiv (g_{\min}, 0) \cup (0, g_{\max}). \tag{38}$$

Second: within this domain it can occur that  $\frac{dz}{dg}$  vanishes. Beyond that point the solution to equation 37 cannot be real and a non zero imaginary part develops with a square-root behaviour. The second case corresponds to the standard square-root singularity at the edge of an eigenvalue distribution.

**Sharp edge** If there exists a point  $g_-^{sh} \in (g_{\min}, 0)$  at which the derivative of the inverse function

$$\frac{dz}{dg} = -\frac{1}{g^2} + \alpha \mathbb{E}\left[\frac{1}{p} \sum_{i=1}^p \frac{c_i^2}{(1 - gc_i)^2}\right]$$
(39)

vanishes, the left edge of the spectrum can be obtained by applying the inverse function to this value, i.e.,  $\lambda_-^{sh} \equiv z(g_-^{sh})$ . The corresponding self-consistent condition is

$$g_{-}^{sh} = -\left\{ \mathbb{E}\left[\frac{1}{p} \sum_{i=1}^{p} \frac{\alpha c_i^2}{(1 - g_{-}^{sh} c_i)^2}\right] \right\}^{-1/2}.$$
 (40)

In this case, the left edge of the spectrum is *sharp*, meaning that the derivative of the eigenvalue density diverges as  $\lambda$  approaches the edge from the right. This behavior arises through a standard square-root singularity at the edge:

$$\rho(\lambda) \underset{\lambda \to \lambda^{sh}}{\propto} (\lambda - \lambda_{-}^{sh})^{1/2}. \tag{41}$$

**Smooth edge** If no solution  $g_-^{sh} \in (g_{\min}, 0)$  exists such that the derivative of z(g) vanishes, that is, if equation 40 cannot be satisfied within the domain of definition—then the left edge of the bulk spectrum is determined by the boundary of the domain itself. In this case, the edge of the resolvent is located at

$$g_{-}^{\rm sm} = g_{\rm min} = \frac{1}{c_{\rm min}},$$
 (42)

and the corresponding spectral edge is given by  $\lambda_-^{sm}=z(g_-^{sm})$ . This edge is referred to as *smooth*, in the sense that the derivative of the spectral density  $\rho(\lambda)$  vanishes as  $\lambda \to \lambda_-^{sm}$ . In our setting, this occurs via an exponential decay of the spectral density near the edge:

$$\rho(\lambda) \underset{\lambda \to \lambda_{-}^{sm}}{\propto} \exp\left[-\frac{A}{(\lambda - \lambda_{-}^{sm})}\right],\tag{43}$$

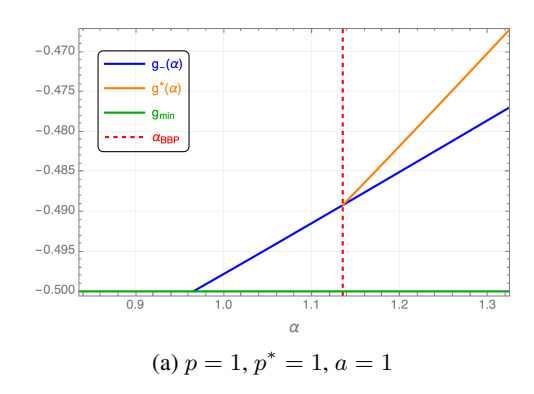
for some constant A>0 (see Bocchi et al. (2025a) for more details about the derivation and the explicit form of the constants), indicating an essential singularity at the edge. In the case of our teacher-student setup, the eigenvalues  $c_i$  are

$$\begin{cases}
c_1 = \frac{2}{p} \frac{1}{a + \frac{1}{p^*} \sum_{j=1}^{p^*} u_j^2} \left( \frac{3}{p} \sum_{i=1}^p \lambda_i^2 - \frac{1}{p^*} \sum_{j=1}^{p^*} u_j^2 \right) \\
c_{2,\dots,p} = \frac{2}{p} \frac{1}{a + \frac{1}{p^*} \sum_{j=1}^{p^*} u_j^2} \left( \frac{1}{p} \sum_{i=1}^p \lambda_i^2 - \frac{1}{p^*} \sum_{j=1}^{p^*} u_j^2 \right),
\end{cases} (44)$$

which have the same support  $c_i \in (-2/p, +\infty) \ \forall i \in [1, p]$ . This implies that for our setting  $g_{min} = -p/2$ . As we increase  $\alpha$ , for fixed values of p,  $p^*$  and a, the left edge goes from being smooth to being sharp. That is, for  $\alpha$  smaller than some value  $\alpha_c$ , the left edge is obtained from equation 42, while for larger  $\alpha$  it is obtained from equation 40. The precise point in which this transition takes places,  $\alpha_c$ , can be determined by imposing the equation

$$-\frac{p}{2} = \left\{ \mathbb{E} \left[ \frac{1}{p} \sum_{i=1}^{p} \frac{\alpha_c c_i^2}{(1 + \frac{p}{2} c_i)^2} \right] \right\}^{-1/2}.$$
 (45)

Depending on the student and teacher number of nodes p,  $p^*$ , as well as the normalizing constant a, either type of transition can occur, as illustrated in Figure 5. In what follows, we present results for  $p^* = 1$ , but we verify in section D of the appendix that varying  $p^*$  does not qualitatively alter the overall picture.



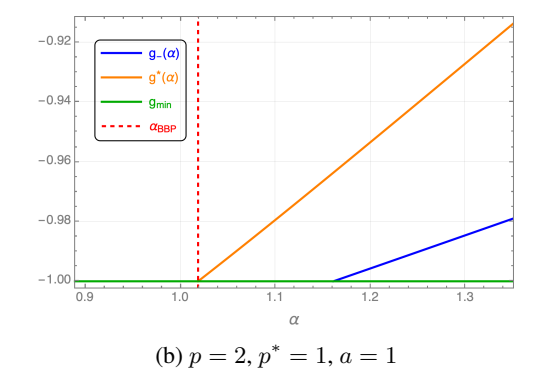


Figure 5: In Panel 5a, a continuous BBP is shown: the  $\alpha_{\rm BBP}$  corresponds to the crossing of the  $g^*(\alpha)$  and  $g_-(\alpha)$  curves. In Panel 5b, a discontinuous BBP is shown: the  $\alpha_{\rm BBP}$  corresponds to the crossing of the  $g^*(\alpha)$  and  $g_{\rm min}(\alpha)$  curves.

Infinite overparametrization limit In this paragraph we consider the limit of infinite overparametrization,  $p \to \infty$ . This limit is taken after the  $N \to \infty$  limit, so we remain in the regime where  $p \ll N$ . We begin by computing the critical value  $\alpha_c$  below which the transition is discontinuous. For large p we can approximate equation 45 as

$$\frac{p}{2} \approx \left\{ \alpha_c \, \mathbb{E} \left[ \frac{4}{p^2} \cdot \frac{\left(1 - \frac{1}{p^*} \sum_l u_l^2\right)^2}{(1+a)^2} \right] \right\}^{-1/2},\tag{46}$$

which yields

$$\alpha_c = \frac{p^*(a+1)^2}{2}. (47)$$

We now turn to the BBP threshold  $\alpha_{\rm BBP}^{p=\infty}(a)$  in the  $p\to\infty$  limit. This expression will be valid only for values of a such that  $\alpha_{\rm BBP}^{p=\infty}(a)<\alpha_c(a)$ . Evaluating equation 36 at  $g^*=-p/2$ , we obtain

$$-\frac{p}{2} = \left\{ \alpha_{\text{BBP}}^{p=\infty} \mathbb{E} \left[ \frac{1}{p} \sum_{i=1}^{p} \frac{c_i(u_1^2 - 1)}{1 + \frac{p}{2}c_i} \right] \right\}^{-1}, \tag{48}$$

which leads to the solution

$$\alpha_{\text{BBP}}^{p=\infty} = \frac{p^*(a+1)}{2}.$$
 (49)

Note that for all a>0, we have  $\alpha_{\rm BBP}^{p=\infty}(a)<\alpha_c(a)$ , implying that the BBP transition is always discontinuous in the  $p\to\infty$  limit. Furthermore, for general  $p^*$ , the minimum of  $\alpha_{\rm BBP}^{p=\infty}(a)$  occurs at a=0 and is equal to  $p^*/2$ , matching the information-theoretic weak recovery threshold identified in Maillard et al. (2024). Note that our setting is far from being Bayes optimal setting as in Maillard et al. (2024) since the overparametrized student, by definition, does not match the teacher structure. Yet, this result shows how powerful overparametrization can be, as in the large overparametrization limit, even simply extracting spectral information from the Hessian at random configurations, the optimal weak recovery threshold is can be achieved.

# C DERIVATION OF THE OVERLAP

In the general multi-index setting, each isolated eigenvalue may correspond to an alignment between a specific student node  $\mathbf{w}_k$  and a teacher node  $\mathbf{w}_l^*$ . We denote the corresponding eigenvectors by  $\mathbf{v}^{kl} \in \mathbb{R}^{pN}$  and reshape them into matrices  $\mathbf{V}^{kl} \in \mathbb{R}^{p \times N}$ , where the first N entries of  $\mathbf{v}^{kl}$  form the first row, and so on.

We define the overlap matrix:

$$\boldsymbol{M}^{kl} = \boldsymbol{V}^{kl} (\boldsymbol{W}^*)^{\top} \in \mathbb{R}^{p \times p^*}, \tag{50}$$

where  $W^* \in \mathbb{R}^{p^* \times N}$  is the matrix whose rows are the teacher weight vectors. Ideally,  $M^{kl}$  contains a single non-zero entry m at position (k, l), i.e.,  $(M^{kl})_{k'l'} = m_{kl} \delta_{k,k'} \delta_{l,l'}$ .

However, the output of the student network in equation 2 can be equivalently written as

$$\hat{y}(\mathbf{x}^{\mu}) = (\mathbf{x}^{\mu})^{\top} \frac{\mathbf{W}^{\top} \mathbf{W}}{p} \mathbf{x}^{\mu}, \tag{51}$$

where  $W \in \mathbb{R}^{p \times N}$  is the matrix whose rows are the student weight vectors. This expression reveals that the output is invariant under rotations of the matrix W in the p-dimensional space. That is, for any orthogonal matrix  $O \in \mathbb{R}^{p \times p}$ , the transformation  $W \mapsto OW$  leaves the output function unchanged. A similar argument applies to the teacher network.

This rotational invariance implies that the student and teacher configurations are only identifiable up to orthogonal transformations, provided that the norms of the student nodes are unconstrained. As a consequence, the overlap matrix observed in practice takes the form

$$\boldsymbol{M}^{kl} = \boldsymbol{O}\boldsymbol{V}^{kl}(\boldsymbol{W}^*)^{\top} \tilde{\boldsymbol{O}}^{\top}, \tag{52}$$

where  $O \in \mathbb{R}^{p \times p}$  and  $\tilde{O} \in \mathbb{R}^{p^* \times p^*}$  are random orthogonal matrices<sup>1</sup>. The scalar overlap m can then be extracted using the Frobenius norm:

$$m_{kl} = \sqrt{\sum_{i,j} \left(M_{ij}^{kl}\right)^2}. (53)$$

Furthermore, due to the symmetry of the problem, all the overlaps will be equivalent:

$$m_{kl} = m \quad \text{for } k = 1, \dots, p, \quad l = 1, \dots, p^*.$$
 (54)

We now derive an analytic equation for m. Let us again choose the teacher vectors such that they are the first  $p^*$  canonical directions, as we already did in the previous section. The starting point is to write the resolvent as

$$G(z) = (z\mathbf{I}_{pN} - \mathcal{H})^{-1} = \sum_{i=1}^{pN} \frac{\mathbf{v}_i \mathbf{v}_i^T}{z - \lambda_i}$$
(55)

where  $\{\lambda_i, v_i\}_{i=1}^{pN}$  is the set of eigenvalues/eigenvectors. Without loss of generality, let us assume that we are in a base in which the first eigenvector is aligned with the first teacher. That is, if we call  $\bar{e}_1$  the first canonical direction in a pN dimensional space, the overlap is  $m = v_1 \cdot \bar{e}_1$ . Multiplying equation 55 on the right and on the left by  $\bar{e}_1$ , and taking the limit  $\lambda \to \lambda^*$  we get that

$$\lim_{z \to \lambda^*} \underbrace{\bar{e}_1^T \left( z \mathbf{I}_{pN} - \mathcal{H} \right)^{-1} \bar{e}_1}_{\tilde{G}_{11}^{11}(z)} = \lim_{z \to \lambda^*} \frac{m^2}{z - \lambda^*}$$
 (56)

The square overlap is the residue of the function  $\tilde{G}_{11}^{11}(z)$  at the pole  $z=\lambda^*$ . Using the relation found in the previous section  $\tilde{G}_{11}^{11}(z)=(z-\Xi(z))^{-1}$ , it can be calculated as

$$m^2 = \lim_{z \to \lambda^*} \frac{z - \lambda^*}{z - \Xi(z)} \tag{57}$$

where we remind the reader that

$$\Xi(\lambda) = \alpha \frac{1}{p} \sum_{i=1}^{p} \mathbb{E}u_1^2 \frac{c_i}{1 - g(\lambda)c_i}.$$
 (58)

This limit gives the undetermined form 0/0, but can be calculated using l'Hopital's rule

$$m^{2} = \lim_{z \to \lambda^{*}} \frac{\partial_{z}(z - \lambda^{*})}{\partial_{z}(z - \Xi(z))} = \frac{1}{1 - \partial_{z}\Xi(z)\big|_{z = \lambda^{*}}}$$

$$(59)$$

<sup>&</sup>lt;sup>1</sup>Note that such orthogonal transformations, while preserving the output, don't preserve the individual norms of the network nodes. If we apply this rotation to the teacher vector, which is taken to be normalized such that each node lies on the  $S_{N-1}(\sqrt{N})$  sphere, such normalization property is lost. However, since the dataset is invariant under this rotation, the student cannot infer this normalization from the data, and will align to a randomly rotated teacher  $\tilde{O}\tilde{W}^*$ .

# D DEPENDENCY ON $p^*$ AND UNDERPARAMETRIZATION

In this appendix we consider cases where  $p^* \neq 1$ . In figure 6 we show the equivalent of figure 2 for  $p^* = 2$ . As we can see the behaviour is qualitatively similar. For the values of p we chose  $\alpha_{BBP}$  is always monotonically decreasing as a function of p, although we don't expect this to hold for larger values of p.

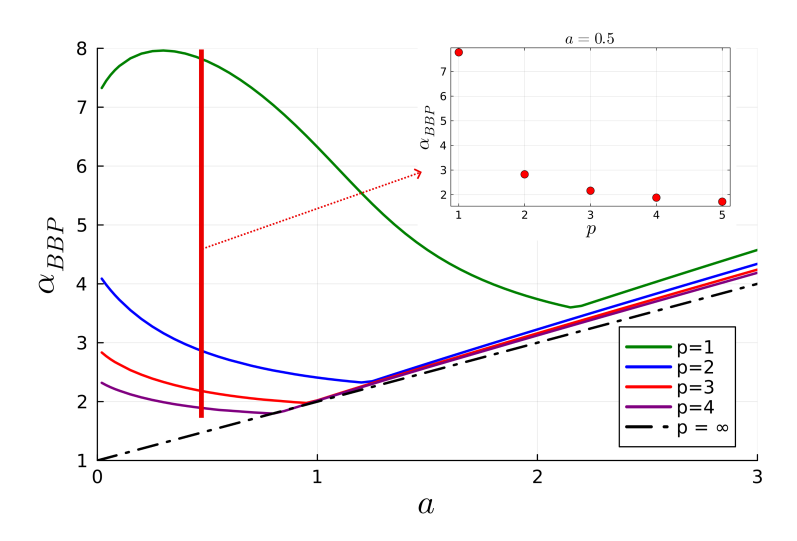


Figure 6:  $\alpha_{BBP}$  as a function of a for  $p^*=2$  for various values of p. In the inset we show  $\alpha_{BBP}$  as a function of p for a fixed value of a=0.5

In figure 7 we explore the effect of underparametrization, by keeping a and p fixed and plotting  $\alpha_{BBP}$  as a function of  $p^*$ . Perhaps unsurprisingly we observe that  $\alpha_{BBP}$  increases, making the problem increasingly harder as the network is more underparametrized.

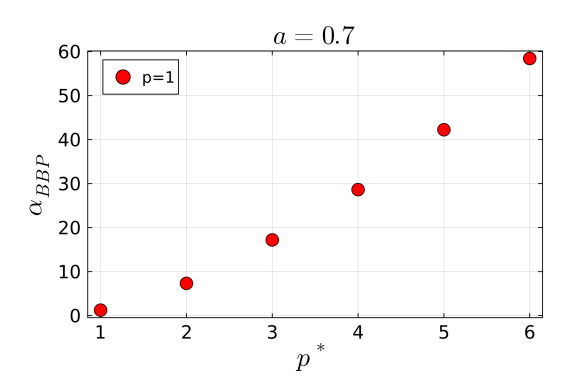


Figure 7:  $\alpha_{BBP}$  as a function of  $p^*$  for p=1 and a=0.7